Articles

Ligand-Induced Changes in the Structure and Dynamics of a Human Class Mu Glutathione *S*-Transferase†

Scott A. McCallum,‡,§ T. Kevin Hitchens,|| Christine Torborg,|| and Gordon S. Rule*,||

Department of Biological Sciences, Carnegie Mellon University, 4400 Fifth Avenue, Pittsburgh, Pennsylvania 15213, and Department of Biochemistry, University of Virginia, Charlottesville, Virginia 22908

Received December 2, 1999; Revised Manuscript Received February 23, 2000

ABSTRACT: Glutathione transferases are detoxification enzymes that catalyze the addition of glutathione (GSH) to a wide variety of hydrophobic compounds. Although this group of enzymes has been extensively characterized by crystallographic studies, little is known about their dynamic properties. This study investigates the role of protein dynamics in the mechanism of a human class mu enzyme (GSTM2-2) by characterizing the motional properties of the unliganded enzyme, the enzyme−substrate (GSH) complex, an enzyme−product complex [*S*-(2,4-dinitrobenzyl)glutathione, GSDNB], and an enzyme−inhibitor complex (*S*-1-hexylglutathione, GSHEX). The kinetic on- and off-rates for these ligands are 10−20-fold lower than the diffusion limit, suggesting dynamic conformational heterogeneity of the active site. The off-rate of GSDNB is similar to the turnover number for its enzymatic formation, suggesting that product release is rate-limiting when 1-chloro-2,4-dinitrobenzene is the substrate. The dynamic properties of GSTM2-2 were investigated over a wide range of time scales using ^{15}N nuclear spin relaxation, residual dipolar couplings, and amide hydrogen−deuterium exchange rates. These data show that the majority of the protein backbone is rigid on the nanosecond to picosecond time scale for all forms of the enzyme. The presence of motion on the millisecond to microsecond time scale was detected for a small number of residues within the active site. These motions are likely to play a role in facilitating substrate binding and product release. The residual dipolar couplings also show that the conformation of the active site region is more open in solution than in the crystalline environment, further enhancing ligand accessibility to the active site. Amide hydrogen−deuterium exchange rates indicate a reduction in the dynamic properties of several residues near the active site due to the binding of ligand. GSH binding reduces the exchange rate of a number of residues in proximity to its binding site, while GSHEX causes a reduction in amide−exchange rates throughout the entire active site region. The location of the dinitrobenzene (DNB) ring in the GSDNB−GSTM2-2 complex was modeled using chemical shift changes that occur when GSDNB binds to the enzyme. The DNB ring makes a number of contacts with hydrophobic residues in the active site, including Met108. Replacement of Met108 with Ala increases the turnover number of the enzyme by a factor of 1.7.

Glutathione *S*-transferases (GSTs)[1] are a family of enzymes that catalyze the conjugation of glutathione (GSH) to a wide range of hydrophobic compounds, including carcinogens and other toxins (see refs *1* and *2* for review). The differential expression of these enzymes has been implicated in the development of cancers as well as their resistance to chemotherapeutic drugs (*3*, *4*). The hallmark of these enzymes is their breadth of substrate specificity. This breadth is achieved by the existence of structurally and functionally distinct classes of mammalian GSTs (alpha, mu, pi, theta, and kappa) and the fact that a single enzyme is

† This work was supported by a grant from the NIH (GM46722) and the Eberly Family Professorship in Structural Biology to G.S.R. The 600 MHz spectrometer was obtained through an equipment grant from the NIH (S100 RR11248-01). NMR studies at 750 MHz were carried out at the National Magnetic Resonance Facility at Madison (operation subsidized by the NIH Biomedical Research Technology Program under Grant RR02301; equipment funded by the University of Wisconsin, NSF Academic Infrastructure Program under Grant BIR-9214394, the NIH Shared Instrumentaion Program under Grants RR2781 and RR08438, the NSF Biological Instrumentation Program under Grant DMB-8415048, and the U.S. Department of Agriculture).

* To whom correspondence should be addressed. E-mail: rule@andrew.cmu.edu. Phone: (412) 268-1839. Fax: (412) 268-7129.

‡ University of Virginia.

§ Current address: Department of Chemistry and Biochemistry, University of Colorado at Boulder, Boulder, CO 80309.

|| Carnegie Mellon University.

[1] Abbreviations: CDNB, 1-chloro-2,4-dinitrobenzene; DNB, dinitrobenzene; GSDNB, *S*-(2,4-dinitrobenzyl)glutathione; GSH, glutathione; GSHEX, *S*-1-hexylglutathione; GST, glutathione *S*-transferase; GSTM2-2, homodimeric human class mu GSTM2; rGSTM3-3, homodimeric class mu GSTM3 from rat; NMR, nuclear magnetic resonance; HSQC, heteronuclear single-quantum coherence; hnNOE, $^{1}H-^{15}N$ heteronuclear NOE.

10.1021/bi992767d CCC: $19.00
Published on Web 06/03/2000

catalytically active toward a number of chemically unique substrates.

The crystal structures of a number of class alpha (*5*−*7*), mu (*8*−*12*), pi (*13*, *14*), and theta (*15*) GSTs have been determined (see ref *16* for review). All cytosolic glutathione transferases are dimeric. Each monomer has an amino terminal α−*β* domain consisting of 70−90 residues, and a larger carboxy-terminal α-helical domain. Glutathione binds at the interface between these two domains but largely contacts residues from the α−*β* domain. The enzymatic mechanism involves Tyr (kappa, mu, and pi)- or Ser (theta)-mediated deprotonation of the thiol group of the bound glutathione, followed by nucleophilic attack of the activated thiol on the hydrophobic substrate (*16*, *17*).

In class mu enzymes, the hydrophobic binding site is composed of four structural elements. The α−*β* domain provides an extended loop (the mu-loop, residues 32−46) that forms one wall of this site. A short peptide segment (residues 9−12) forms the floor of the hydrophobic binding site. The α-helical domain contributes the carboxy terminus of the fourth helix (D-helix, residues 104−116) and the 10-residue carboxy-terminal Ω-loop to the hydrophobic binding site. Residues in GSTM2-2 that potentially interact with hydrophobic substrates are Leu12, Met34, Met104, Met108, Ala111, Tyr115, Phe208, Thr209, and Met211. A similar set of residues are found in the homologous class mu enzyme from rat (rGSTM3-3), the exception being that Ala111, Thr209, and Met211 are replaced with Ile, Ser, and Leu, respectively.

With the exception of the conserved D-helix and the floor of the hydrophobic binding site, the topology of the active site region is significantly different for each enzyme class. Class pi, alpha, and theta enzymes all contain a short helix near the glutathione binding site (helix α2) that replaces the mu-loop found in class mu enzymes. The carboxy terminus of the class pi enzyme is shorter than that found in class mu enzymes. In class alpha and theta enzymes, the carboxy terminus forms an α-helix that covers the active site.

The structural topologies of the class mu, alpha, and theta enzymes indicate that some degree of conformational mobility is required for substrate binding and product release. In the case of class mu enzymes, crystal structures show that the mu-loop, the D-helix, and the carboxy-terminal Ω-loop partially occlude the active site region, blocking access of substrates and release of product. High temperature factors (30−60 Å^2) for these regions suggest that these conformations may be transitory (*9*). Previous crystallographic studies of the human class mu enzyme, GSTM2-2, suggested that the Ω-loop may assume different conformations in solution (*9*). However, subsequent NMR studies showed that a single conformation is predominate (*18*). Heteronuclear NOE measurements indicated that the Ω-loop is rigid on the picosecond to nanosecond time scale (*18*). Thus, the high temperature factors of the Ω-loop are due to the existence of a number of structurally similar conformational states that interchange slowly.

Other classes of GSTs also exhibit high temperature factors for regions near the active site. In the unliganded class pi enzyme, the temperature factors for residues in helix α2 exceed 50−60 Å^2. The binding of GSH lowers these temperature factors to 20−50 Å^2 (*13*). The carboxy-terminal α-helix of the human class alpha enzyme, GSTA2-2, also undergoes a similar disorder−order transition when binding glutathione conjugates (*6*). These observations suggest that ligand binding may induce a single stable conformation of the active site in both class alpha and pi GSTs. The human class alpha enzyme, GSTA4-4, may be an exception to this generalization since its carboxy-terminal helix appears to be ordered in the absence of bound ligand (*5*).

Individual residues may also play a role in gating access to the active site. A crystallographic study of several intermediates in the reaction of GSH and 1-chloro-2,4-dinitrobenzene (CDNB) has been performed for a class mu enzyme from rat (rGSTM3-3; *12*). The structure of rGSTM3-3 was determined in complex with a transition state analogue [1-(*S*-glutathionyl)-2,4,6-trinitrocyclohexadienate anion, GSTNB] and product [*S*-(2,4-dinitrobenzyl)glutathione, GSDNB]. In the GSTNB complex, the trinitrobenzene ring is located above the floor of the hydrophobic binding site and below residues Tyr115 and Ser209. Tyr115 and Ser209 interact via hydrogen bonding and appear to form a cap above the trinitrobenzene ring. Replacement of Tyr115 with Phe increases both the turnover number and the off-rate of GSDNB, suggesting that the interaction between Tyr115 and Ser209 is functionally important in rGSTM3-3 (*19*). The interaction between equivalent residues in GSTM2-2 (Tyr115 and Thr209) is less important for catalysis; the specific activity of the Tyr115 to Phe mutant is similar to that of the wild-type enzyme (*20*).

This study investigates the role of protein dynamics in the catalytic function of a human class mu enzyme, GSTM2-2. Protein dynamics can influence the enzymatic mechanism of GSTs in several ways. First, the rate of ligand binding can be influenced by the interconversion of conformational states that have different intrinsic binding properties. Second, the release of product may require the transient opening of the active site region. Third, the broad substrate specificity of these enzymes can be generated from changes in the conformation of either the main chain or side chain atoms. These distinct conformations can have different binding affinities for different hydrophobic substrates. Finally, a reduction in the number of protein conformations by substrate binding can be used to store free energy early in the catalytic cycle which can later be used to enhance product release.

The characterization of the dynamic properties of a protein involves assessing the structural variability of significantly populated conformational states and determining the rate of interconversion between these states. One method of demonstrating the existence of structural variability is to compare the kinetic on-rate of substrates to the rate expected from the diffusion limit. If multiple conformations exist, with different binding properties, then the kinetic on-rate will be lower than the diffusion limit. In this regard, the characterization of ligand binding kinetics provides important information about the role of dynamics in enzyme function. Kinetic on-rates for all ligands studied here were 10−20-fold lower than the diffusion limit. Furthermore, the kinetic off-rate of a product, GSDNB, was found to be close to the turnover rate of the reaction. These results strongly indicate that protein dynamics influences the catalytic mechanism of this class mu enzyme.

The motional properties of GSTM2-2 were characterized for several different enzyme−ligand complexes: unliganded enzyme, an enzyme−substate complex (GSH), an enzyme−

product complex (GSDNB), and an enzyme−inhibitor complex (*S*-hexylglutathione, GSHEX). These different enzyme forms allowed the characterization of the dynamic properties of GSTM2-2 at various steps of the catalytic cycle. High-frequency (picosecond to nanosecond) motions were investigated using ^{15}N nuclear spin-relaxation methods. ^{15}N relaxation has been extensively used to characterize the dynamic properties of proteins (see refs *21* and *22*). Using the model-free approach developed by Lipari and Szabo (*23*, *24*), it is possible to obtain information about the amplitude (order parameter, S^2) and the correlation time for internal motion (τ_F). Although there has been some reservation regarding the physical interpretation of the Lipari−Szabo model (*21*), it is a suitable approach for characterizing ligand-induced *changes* in dynamics, which is the principle focus here. Lower-frequency motions were investigated in this study by measuring the proton−nitrogen residual dipolar coupling in partially oriented samples of GSTM2-2. The use of residual dipolar couplings in structure determination was pioneered by Bothner-By (*26*) and is now widely used in the determination of protein (*27*) and nucleic acid structures (*28*). These couplings can also be used as a measure of the dynamic properties of the protein (*29*). Motions that are faster than the time scale of the coupling (microsecond) lead to averaging of the dipolar coupling.

Motions that occur more slowly than the microsecond time scale can be inferred from amide−hydrogen exchange rates (*30*). Residues with slowly exchanging amide hydrogen atoms either are buried in the protein or participate in hydrogen bonding. Fluctuations of the structure allow these amide sites to sample a manifold of conformations, some of which permit exchange with the solvent (*31*, *32*). Therefore, amide exchange rates can reflect dynamic motions or structural flexibility of the protein over a wide range of time scales. A ligand-induced decrease in exchange rates implies a reduction in the number of conformational states of the protein in the protein−ligand complex (*33*, *34*).

On the basis of the data presented here, the influence of dynamics on the rate of substrate binding and product release in GSTM2-2 is restricted to motions that are slower than microseconds. The nuclear spin-relaxation data indicate that the peptide backbone does not undergo rapid or large structural fluctuations on the nanosecond to picosecond time scale. The residual dipolar couplings indicate that only the mu-loop exhibits conformational averaging on the microsecond time scale. Amide exchange measurements indicate that both the D-helix and the carboxy-terminal Ω-loop undergo a ligand-induced reduction in amide exchange kinetics.

The availability of resonance assignments for protein−ligand complexes permitted an investigation of the environment of the hydrophobic moiety of bound products. Structural models of the GSDNB−GSTM2-2 complex suggested a functional interaction between the DNB ring and Met108. The changes in the steady-state kinetic parameters that occur when Met108 is replaced with Ala support this conclusion.

MATERIALS AND METHODS

Sample Preparation and Enzyme Assays. Samples of GSTM2-2 were prepared using previously described isotopic labeling schemes (*18*). All isotopes were purchased from Cambridge Isotopes Laboratories, Inc. (CIL, Andover, MA). Perdeuterated and ^{13}C- and ^{15}N-labeled protein were prepared using Bio-Express cell growth medium (CIL). GSTM2-2 deuterated to a level of 85% was used for all experiments except where noted. This level of deuteration was achieved by growing the *Escherichia coli* host in minimal medium containing 4 g/L glucose, 1 g/L ammonium sulfate, and 98% ^2H_2O (see ref *18* for details). Isotopic labeling was achieved using [^{15}N]ammonium sulfate and protonated [^{13}C]glucose. Samples specifically labeled at the carbonyl carbon were also prepared as described previously (*18*). NMR samples were in 10 mM potassium phosphate (pH 7.0), 50 mM sodium chloride, 1 mM dithiothreitol, 0.02% sodium azide, and 5% ^2H_2O. Protein concentrations were approximately 1.3 mM (monomer) with the exception of those of the Pf1 phage-oriented samples, which were approximately 0.7 mM. The Pf1 bacteriophage was prepared as described by Hansen et al. (*48*).

GSH, CDNB, and GSHEX were purchased from Sigma Chemical Co. GSDNB was prepared from GSH and CDNB (*35*), and its concentration was determined spectrophotometrically ($\epsilon_{340} = 8300\ M^{-1}\ cm^{-1}$; *35*). GSDNB and GSH stock solutions (100 mM) were prepared in NMR buffer and added directly to unliganded GSTM2-2 to provide a final ligand concentration of 5.0 mM. GSHEX samples were prepared by the addition of 5 mL of 6 mM GSHEX to 0.3 mL of GSTM2-2. This solution was concentrated 10-fold by ultrafiltration (Centricon-10 units, Amicon), and the procedure was repeated to give the final NMR sample.

The Met108 to Ala mutation was introduced using the method described by Kunkel (*36*). Steady-state kinetic parameters were obtained by measuring initial rates at the following combinations of substrate concentrations: GSH (0.05, 0.1, 0.5, and 1 mM) and CDNB (0.1, 0.5, and 1.0 mM) in 0.1 M phosphate buffer (pH 7.0) at room temperature (*37*). Steady-state parameters for an ordered steady-state mechanism (V_{max}, K_{iGSH}, K_{mCDNB}, and K_{mGSH}; *38*) were obtained by nonlinear least-squares fitting of the initial reaction velocity using the program NONLIN (*39*).

NMR Spectroscopy. NMR spectra were recorded at 600 or 750 MHz using Bruker DMX spectrometers equipped with deuterium decoupling and Bruker triple-resonance probes with triple-axis pulsed field gradient coils. All spectra were recorded at 298 K. Homonuclear NOE mixing times were 100−150 ms. Quadrature detection was obtained using the States−TPPI method (*40*). The recycle delay for most NMR experiments was 1.3 s. Pulsed field gradients were used to suppress undesired coherences and water magnetization (*41*). Water suppression schemes generally included gradients applied as ZZ-filters and a "watergate" selection for off resonance signals (*42*). The following triple-resonance experiments were used for resonance assignment purposes: HNCA, HN(CO)CA, HN(CA)CB, HN(COCA)CB, HN(CACB)CG, HN(COCACB)CG, HNCO, and HN(CA)CO. NMR spectra were processed and analyzed as described previously (*18*) using FELIX 97.0 (Molecular Simulations Inc., San Diego, CA) software on a R4400 Silicon Graphics workstation.

Chemical Shift Assignments. Chemical shift assignments of the GSH-, GSDNB-, and GSHEX-bound complexes were obtained utilizing a modified version of the Monte Carlo algorithm that was previously used to assign those of

unliganded GSTM2-2 (*18*). The key difference here is that the program was modified to use the assignments of unliganded enzyme as an additional source of information. This modification reduces the number of connectivities and amount of residue type information required to obtain unambiguous assignments of the complexes.

In the initial runs of the assignment program, similarities of the chemical shifts in the GST complexes and unliganded enzyme were weighted heavily in the scoring scheme. Most residues were assigned with a high degree of certainty using this strategy. Subsequent runs of the program used lower weightings and wider chemical shift tolerances for the matching of liganded and unliganded chemical shifts. This approach allowed those residue atoms that undergo large changes in resonance frequencies upon ligand binding to be weighted less significantly by the known chemical shifts of the unliganded protein. It is possible that this assignment strategy may bias the assignment of the complex toward solutions that are similar to that of the unliganded chemical shifts. However, identical assignments for the GSDNB−GSTM2-2 complex were obtained regardless of whether assignments from the unliganded complex were used.

Calculation of Ligand-Induced Chemical Shift Changes. Expected changes in amide proton chemical shifts due to ring currents from the presence of the DNB ring were calculated using the program *shifts* (*43*). The ligand parameter files provided with the program were expanded to include descriptions for GSH and GSDNB. Coordinates and partial charges for these ligands were obtained from XPLOR parameter files. The ring current parameters for the dinitrobenzene (DNB) ring were taken to be the same as those of benzene. The coordinates for the GSH−GSTM2-2 complex were obtained by removal of the DNB ring from the GSDNB−GSTM2-2 structure.

Line Shape Analysis. ^{1}H−^{15}N HSQC (*44*) spectra (8−32 scans/t_1 point) were recorded at 600 MHz on samples that contained various concentrations of GSH (0.21−7.68 mM), GSDNB (0.12−4.75 mM), and GSHEX (0.09−6.67 mM). Accurate fitting of the resonance line shape was only possible for resolved peaks with observable line shapes for most points of the titration. For amides whose resonance peak exhibited ligand-induced changes in chemical shift in both dimensions, it was necessary to remove the effect of exchange broadening in the nitrogen dimension before fitting the proton line shape. This was accomplished by summing all of the one-dimensional ^{15}N slices that contained the proton signal of interest.

The ligand on- and off-rate constants were determined by global fitting of all the spectra acquired at different ligand concentrations to the general equation for chemical exchange (*45*, *46*):

$$G(\omega) = I\frac{f_A[\omega_B + i(\gamma_B + k_1[S])] + f_B[\omega_A + i(\gamma_A + k_2)]}{(\omega_A\omega_B + k_1[S]k_2 - \gamma_A\gamma_B) + i(\omega_A\gamma_B + \omega_B\gamma_A)} \quad (1)$$

where I is the amplitude, k_1 is the microscopic on-rate, k_2 is the microscopic off-rate, f_A and f_B are the fractions of the spin in states A (unliganded) and B (liganded), respectively, [S] is the free substrate concentration, $\omega_A = \omega - \omega^o_A$, and $\omega_B = \omega - \omega^o_B$, where ω^o_A and ω^o_B are the resonance frequency of states A and B, respectively, and $\gamma_A = k_1[S] + 1/T_{2A}$ and $\gamma_B = k_2 + 1/T_{2B}$, where T_{2A} and T_{2B} are the transverse relaxation times for the spin in states A and B, respectively.

Acquisition and Analysis of Relaxation Data. T_1, T_2, and hnNOE measurements were performed at 600 and 750 MHz using sequences based on those reported by Farrow et al. (*47*). The quadrature detection scheme was modified from "sensitivity enhancement" to the States−TPPI method. The States−TPPI detection method was found to improve sensitivity because of the reduced time that ^{1}H and ^{15}N magnetization is transverse. The spectral resolution and sensitivity of these sequences were increased by the incorporation of a semiconstant time scheme for ^{15}N chemical shift evolution. Because of the small T_2 values in GSTM2-2, it was necessary to modify the CPMG scheme in the T_2 pulse sequence to reduce the minimum pulse train from 14 to 3.6 ms. This modification retains proton inversion to average cross-correlation while allowing adequate sampling of the T_2 values in GSTM2-2. A total of 32 scans/t_1 point were averaged for the hnNOE experiments. Spectra were recorded with 32 scans (T_1 and T_2) at 600 MHz and 16 (T_1) and 24−32 (T_2) scans at 750 MHz. The proton spectral width was 15 ppm at both field strengths. The nitrogen spectral width was 30.4 and 27.2 ppm at 600 and 750 MHz, respectively. A total of 120−140 t_1 (nitrogen) and 1024 t_2 (proton) complex points were recorded for all experiments.

A total of eight relaxation delays were obtained for the T_1 and T_2 measurements. The relaxation delays in T_1 measurements ranged from 0.0 to 4.2 s, and the delays in the T_2 experiments ranged from 0.0 to 75.6 ms. In the case of the ^{1}H−^{15}N heteronuclear NOE (hnNOE) experiments, the recycle delay between scans was 8.5 and 6.0 s at 600 and 750 MHz, respectively, including a 3.4 s presaturation period. The shorter recycle delay at 750 MHz was a consequence of time limitations for data collection.

T_1 and T_2 intensity data were fit to an exponential decay function using NONLIN. The hnNOE was calculated as a ratio of the peak intensities from spectra with and without proton presaturation. The error in the data was taken to be the sum of the peak-to-peak noise intensity. The ^{15}N relaxation parameters were analyzed using the Modelfree (version 4.0) software package according to the protocol reported by Palmer and co-workers (*25*).

Residual Dipolar Coupling. Pf1 filamentous bacteriophage were used to induce the magnetic alignment of unliganded GSTM2-2 and the GSHEX−GSTM2-2 complex. The final bacteriophage concentration was 9 mg/mL for the unliganded protein and 14 mg/mL for the GSHEX complex. A J_{NH}-modulated HSQC experiment (*49*), acquired at 600 MHz, was used to determine the ^{1}H−^{15}N coupling constants for the unliganded protein without phage, the unliganded protein with phage, and the GSHEX complex with phage. A set of 10 two-dimensional HSQC spectra (128 complex points in t_1) were recorded with evolution of ^{1}H−^{15}N coupling varying between 0.5 and 13.5 ms. The J_{NH} coupling was obtained by fitting the peak amplitudes to an exponentially decaying cosine function using NONLIN. The standard error in the residual dipolar coupling was 1.9 and 3 Hz for the unliganded protein and the GSHEX−GSTM2-2 complex, respectively.

Comparison of experimentally measured ^{1}H−^{15}N coupling constants and those predicted from the X-ray structures was

performed using in-house software. The residual dipolar coupling was calculated using the following relationship (*27*):

$$D_{ij}(\theta,\phi) \propto -S[A_a(3\cos^2\theta - 1) + {}^3/_2 A_r \sin^2\theta \cos 2\phi] \quad (2)$$

where D_{ij} is the residual dipole coupling, A_a and A_r are the axial and rhombic components of the molecular alignment tensor, respectively, S is the generalized order parameter for internal motion of the amide bond vector, and θ and ϕ are the spherical coordinates describing the orientation of the ij vector in the principal axis system of the molecular alignment tensor.

The predicted dipolar couplings were obtained by systematically rotating the protein through all possible orientations. For each of these orientations, the axial and rhombic components of the orientation tensor were obtained by averaging the contribution from equivalent residues in each monomer and then minimizing the difference between observed and predicted coupling. The orientation of the alignment tensor that gave the smallest χ^2 value was used to calculate the predicted couplings. Since small values of the dipolar coupling can represent significant local mobility, the χ^2 was weighted by the value of the experimental dipolar coupling. In addition, residues with high crystallographic temperature factors (residues 34−43, 113−118, and 203−217) were not used in calculating the orientation tensor.

Molecular Mechanics Calculations. Constrained molecular mechanics calculations were performed using X-PLOR, version 3.851 (*50*). A set of amide−amide and amide−H^β distances were used to constrain regions of the molecule with low crystallographic temperature factors. The distance range that a pair of atoms could sample was set to the sum of the temperature factor (in square angstroms) for the pair of atoms divided by 100. These constraints allowed extensive movement of the mu-loop, the top of the D-helix, and the carboxy terminus but kept the remaining portion of the molecule fixed during the calculation. Calculations were performed at 100 K for 10 ps. The protein was then cooled to 50 K over 10 ps and then subject to 400 steps of energy minimization.

Amide Exchange Measurements. Unliganded GSTM2-2 was prepared for deuterium exchange measurements by three cycles of adding 5 mL of ^2H_2O containing NMR buffer to a 0.3 mL volume of GSTM2-2, followed by concentration of the sample to approximately 0.5 mL. Two-dimensional HSQC spectra were acquired at 600 MHz at various times after exchanging the protein into ^2H_2O. A total of 28 spectra were acquired in series for the first 32 h of exchange. The first 10 spectra were acquired every 20 min (4 scans/t_1), followed by 10 every 40 min (8 scans/t_1), and then 6 every 100 min (16 scans/t_1), and the last 2 were acquired for 400 min (64 scans/t_1). A final spectrum was obtained after exchange for 80 h (32 scans/t_1). Peak intensities were corrected for differences in signal averaging and fit to an exponential decay using NONLIN.

Crystallographic Refinement. Structure refinement was initiated using the 2.55 Å structure of unliganded GSTM2-2 (2gtu; *8*). All of the waters in the original GSDNB−GSTM2-2 model (1hna; *9*), with the exception of three water molecules in the active site region, were also used. The location of the glutathione moiety of GSDNB was identical to that observed in the earlier structure of GSTM2-2, and the initial placement of the DNB ring was based on chemical shift data. The unliganded structure was chosen over the original GSDNB−GSTM2-2 structure to reduce map bias toward the previous GSDNB−GSTM2-2 refinement. Refinement consisted of 10 cycles that included simulated annealing using X-PLOR (25 ps at 1000 K followed by cooling to 300 K, 25 K drop/25 ps), manual adjustment of the structure, addition of water molecules, and temperature factor refinement. Additional atoms in the final model consisted of the DNB ring and 23 water molecules. The final *R*-factor was 20.1%, 0.6% less than the original *R*-factor (*9*).

RESULTS AND DISCUSSION

Chemical Shift Assignments. Approximately 180 amide resonances are observed in the spectra of GSTM2-2. The remaining amide sites back-exchange too slowly after purification from the deuterated growth media to be observed. It was possible to assign 173 (96%) of these amides in the GSDNB−GSTM2-2 complex. Assignments were attained using i and $i - 1$ C^α, C^β, C^γ, and CO connectivities to the amides. In addition, a limited number of residue specific assignments were obtained by using samples that were labeled at 1-^{13}C with either Leu, Lys, or Phe (*18*). Amide−amide NOE connectivities were also used to confirm some assignments. The assignments of 171 amide resonances in the GSHEX−GSTM2-2 complex were obtained using H^N, N^H, C^α_i, C^α_{i-1}, C^β_i, C^β_{i-1}, and CO_{i-1} chemical shifts as well as amide−amide connectivities from NOESY experiments. The backbone assignments of the GSH−GSTM2-2 complex were obtained with the fewest number of carbon connectivities: C^α_i, C^α_{i-1}, and CO_{i-1}. These were supplemented with amide−amide connectivities to yield a total of 161 unambiguous amide assignments.

Chemical Shift Mapping of the Ligand Binding Site. Binding of GSH resulted in large changes in amide proton chemical shifts (e.g., 0.3−0.8 ppm) for residues 70−73. Smaller changes (e.g., 0.1−0.3 ppm) for residues 44−52, 57, 58, and 103−106 (see Figure 1A). The larger changes reflect close association between the carboxyl group of the γ-Glu moiety of GSH and residues 70−73. Residues 44−52, 57, and 58 are located next to the carboxy group of the Gly moiety of GSH.

The binding of GSH also perturbs the environment of the base of the D-helix (residues 100−106) and to a lesser extent the carboxy-terminal Ω-loop and residues in the floor of the active site (residues 9−12). While many of these chemical shift changes may result from electrostatic interactions with the activated thiol of bound glutathione, those observed for residues in the D-helix are likely due to a reorientation of the two domains upon GSH binding. This conclusion is supported by the detection of similar chemical shift changes for the D-helix residues when either GSDNB or GSHEX is bound. Furthermore, as discussed below, a small rotation of the two domains is detected in the crystal structures of the unliganded and GSDNB complex of GSTM2-2.

Changes in chemical shift induced by binding of GSDNB or GSHEX are shown in Figure 1. Note that these difference plots highlight chemical shift changes that are induced by the hydrophobic moiety of the ligand. Both GSDNB and GSHEX produced chemical shift changes in the upper portion of the D-helix and in the lower part of the carboxy-

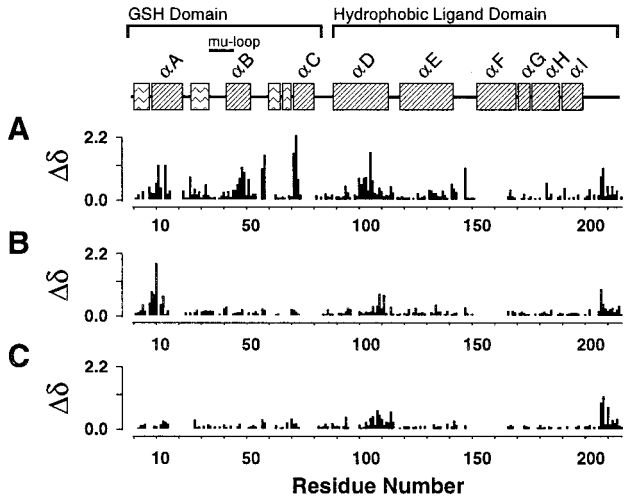

FIGURE 1: Ligand-induced chemical shift changes for different residues in GSTM2-2. The secondary structure and domain organization of GSTM2-2 are shown at the top of the figure. β-Sheets are represented by unlabeled boxes filled with horizontal waved lines. α-Helices are represented by labeled boxes filled with oblique lines. Panel A shows the difference in chemical shifts, $\Delta\delta$, between the GSH−GSTM2-2 complex and the unliganded enzyme. Panel B or C shows the difference in the amide chemical shifts between GSDNB or GSHEX and GSH, respectively. The differences in both the amide proton and nitrogen shifts are plotted [$\Delta\delta = (\delta H^2 + \delta N^2)^{1/2}$]. $\Delta H = \delta_H X - \delta_H Y$, and $\Delta N = \delta_N X - \delta_N Y$, where X is GSH, GSDNB, and GSHEX in panels A−C, respectively, Y is no ligand (panel A) or GSH (panels B and C).

terminal segment (residues 205−210) beyond those seen with GSH binding. These chemical shift changes suggest that the binding sites of both ligands overlap and are nestled between the D-helix and the carboxy terminus. These regions have been identified as being part of the hydrophobic binding site from crystallographic data (*10*−*12*). The observed chemical shift changes may reflect a combination of the direct contact between the hydrophobic moiety of the protein and small structural changes required to accommodate the hydrophobic moiety of GSDNB or GSHEX. The largest chemical shift change in the carboxy-terminal segment is found for residue Thr209. This large change probably reflects movement of the side chain of Phe208 due to the presence of either the hexyl group or the DNB ring. These chemical shift perturbations can also be due to a change in the orientation of Tyr115 that occurs due to ligand binding (*9*, *20*).

Several residues in the floor of the active site exhibit chemical shift changes that are specific to the binding of GSDNB. Large changes in amide proton chemical shifts are observed for Arg10 (−0.27 ppm), Gly11 (−0.63 ppm), and Ala13 (−0.33 ppm). Leu12 must also undergo a large chemical shift change since this residue could not be assigned in the GSDNB complex due to exchange broadening. This clustering of chemical shift changes suggests that the DNB ring is positioned near the floor region of the hydrophobic binding site.

Placement of DNB by Crystallography and Chemical Shift Calculations. In the original electron density map of GSTM2-2, the density associated with the DNB moiety of GSDNB was weak and disjointed (*9*). Therefore, the placement of the DNB ring on the basis of this density alone was considered unreliable. The chemical shift data presented above suggest a location of the DNB ring that is consistent with the poorly defined electron density in the active site region. This prompted additional refinement of the previous 1.8 Å structure (1hna).

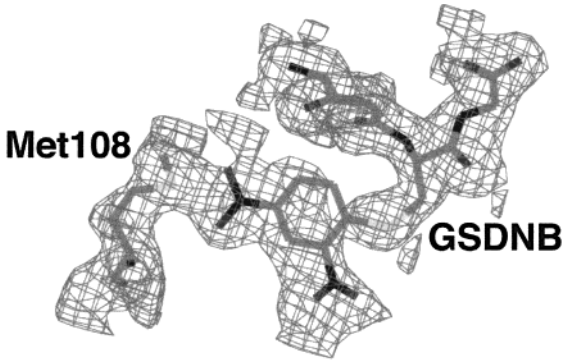

FIGURE 2: Location of the DNB ring by X-ray crystallography. The electron density map (contoured at 0.6σ) in the region of the bound GSDNB and Met108 is shown.

During this refinement it became apparent that the conformation of residues 204−206 in the original GSDNB−GSTM2-2 structure was in error and that the conformation of these residues is similar to that observed in the unliganded GSTM2-2 structure (2gtu). However, as in the earlier refinement of the GSDNB−GSTM2-2 complex, the electron density for residues 204−217 was still difficult to interpret. Consequently, the conformation of the carboxy-terminal Ω-loop is still poorly defined by the electron density. However, the overall chain tracing of residues 207−217 remains similar to that reported previously for the X-ray (*9*)- and NMR (*18*)-derived structures of this region.

The electron density map in the region of the DNB ring is shown in Figure 2. Although the density for the ring atoms is broken, the two NO_2 groups are in regions of high electron density. The location of the DNB ring is substantially different from that reported for the complex between GSDNB and a homologous class mu enzyme from rat (rGSTM3-3; *12*). In the rGSTM3-3 structure, the DNB ring projects into the intermonomer cleft and does not contact any residues in the hydrophobic binding site (see Figure 3).

To determine whether the observed chemical shifts were consistent with the location of the DNB ring in the GSDNB−GSTM2-2 complex, shifts were calculated for a number of different models of the DNB ring. These models included the orientation of the DNB ring as described for rGSTM3-3, the orientation of the DNB ring in the re-refined GSTM2-2 X-ray structure (model 1 in Table I), or an alternative conformation of the DNB ring which was generated by rotation about the $S^\gamma-C^\delta$ bond (model 2 in Table 1). The difference between the calculated chemical shifts of the GSH and GSDNB complexes was compared to the observed shift differences (see Table 1). Neither of the first two locations (rGSTM3-3 and model 1) produced calculated shifts that were similar to the observed chemical shift differences. However, rotation of the DNB ring by ≈50° about the $S^\gamma-C^\delta$ bond improved the agreement between observed and calculated shifts (see model 2 in Table 1).

The quantitative agreement between the calculated and observed shifts is poor. This is likely due to errors in the ring current parameters as well as to subtle changes in the orientation of the aromatic rings of Tyr115 and Phe208 that

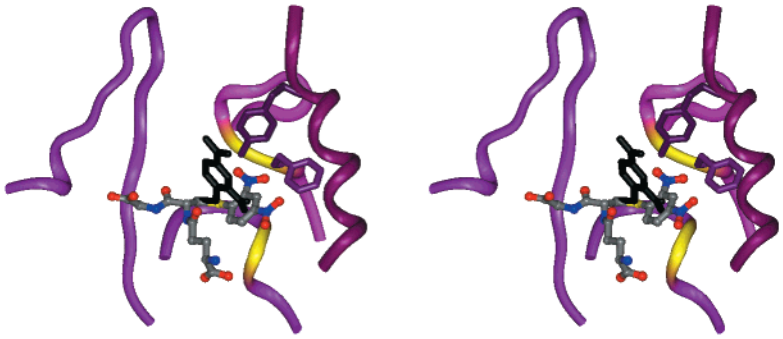

FIGURE 3: Location of the dinitrobenzene ring. A stereoview of the active site region of GSTM2-2 is shown. The protein chain is rendered as a solid ribbon. The purple loop on the left is the mu-loop. The dark purple helix in the foreground represents residues 102−116 of the D-helix. Behind this helix are residues 204−217 of the carboxy terminus (colored in lighter purple). The remaining purple segment represents the floor of the hydrophobic binding site (residues 6−14). The side chains of Tyr115 and Phe208 are also shown, colored in dark purple. The GSDNB molecule, in the orientation determined by analysis of the GSDNB-induced chemical shift changes, is rendered as a ball-and-stick model (CPK coloring). The orientation of the DNB ring in the rat 3-3 enzyme as described by Ji et al. (*12*) is rendered as sticks and colored black. Residues that show a large change in amide proton chemical shifts due to GSDNB binding are colored yellow.

Table 1: GSDNB Proton Chemical Shift Changes[a]

residue no.	observed shift (ppm)	rGSTM3-3	GSTM2-2 model 1[b]	GSTM2-2 model 2
10	−0.27	0.00	0.06	−0.04
11	−0.63	0.00	0.11	−0.10
13	−0.33	0.08	−0.12	−0.08

[a] All chemical shifts are reported as differences between the shifts observed in the GSDNB complex and the shifts observed in the GSH complex. [b] Model 1 is the orientation of the DNB ring in the refined crystal structure of GSTM2-2. Model 2 is obtained from model 1 by a 50° rotation of the DNB ring clockwise about the $S_\gamma-C_\delta$ bond.

Table 2: Steady-State Kinetic Parameters for GSTM2-2 and the Met108 → Ala Mutant

parameter[a]	GSTM2-2	Met108 → Ala
turnover no.	$220 \pm 19\ s^{-1}$	$375 \pm 77\ s^{-1}$
K_{iGSH}	$(7.80 \pm 5.50) \times 10^{-5}$ M	$(3.90 \pm 1.90) \times 10^{-5}$ M
K_{mCDNB}	$(0.34 \pm 0.08) \times 10^{-3}$ M	$(2.20 \pm 0.70) \times 10^{-3}$ M
K_{mGSH}	$(4.30 \pm 2.60) \times 10^{-5}$ M	$(10.00 \pm 7.10) \times 10^{-5}$ M
V_{max}/K_{mGSH}	$(5.0 \pm 3.0) \times 10^{6}\ M^{-1}\ s^{-1}$	$(4.0 \pm 3.0) \times 10^{6}\ M^{-1}\ s^{-1}$
V_{max}/K_{mCDNB}	$(6.5 \pm 0.2) \times 10^{5}\ M^{-1}\ s^{-1}$	$(1.8 \pm 0.6) \times 10^{5}\ M^{-1}\ s^{-1}$

[a] See Segel (*38*) for nomenclature.

occur upon ligand binding. The orientation of these rings within the protein may contribute to the changes in the chemical shifts of residues 10 and 11. Nevertheless, these data indicate that the position of the DNB ring in the GSDNB−GSTM2-2 complex is different from the position described in the structure of the homologous class mu enzyme, rGSTM3-3, for two reasons. First, the experimental chemical shift changes for residues 10, 11, and 13 are negative, as predicted by the orientation of model 2. Second, these calculations indicate that the position of the DNB ringin the GSDNB−rGSTM3-3 complex is too distant to affect the chemical shifts of residues 10−13.

The position of the DNB ring in GSTM2-2 is very similar to the position of the trinitrobenzene ring reported for the complex between rGSTM3-3 and the transition state analogue, GSTNB. The fact that the protein−ligand interactions for both the transition state analogue and GSDNB include residues in the floor of the hydrophobic binding site suggests that CDNB also binds at this site in GSTM2-2. The different location of the DNB ring in the GSDNB−rGSTM3-3 complex may be due to the substitution of Ala111 in GSTM2-2 with Ile in rGSTM3-3. This change makes the binding site more crowded in the rGSTM3-3 complex, perhaps favoring exclusion of the DNB ring.

Role of Met108 in CDNB Binding. The position of the DNB ring in the GSDNB complex shows a close association between the sulfur atom of Met108 and the *p*-NO_2 group of the DNB ring. Consequently, Met108 may play a key role in the binding of CDNB. This hypothesis was tested by replacing Met108 with Ala and determining the effect of this change on the steady-state kinetic parameters of the enzyme. Substitution of Met108 with Ala did not change the steady-state mechanism (ordered steady state) or the binding of GSH (see Table 2). In an ordered steady-state mechanism, the kinetic on-rate for the binding of GSH, k_1, is equal to V_{max}/K_{mGSH}, and the dissociation constant for GSH is equal to the steady-state constant K_{iGSH}. The data presented in Table 2 show that there is no significant difference in either of these parameters between the wild-type and mutant protein.

The affinity of CDNB cannot be directly obtained from the steady-state kinetic rate constants. However, under the assumption that the reverse rate constant is small, V_{max}/K_{mCDNB} is (*38*) as follows:

$$\frac{V_{max}}{K_{mCDNB}} = \frac{k_2 k_p}{k_{-2} + k_p} \qquad (3)$$

If Met108 only participates in the binding of CDNB, but not the chemical step, then k_P would be the same for both the mutant and wild-type protein. In this case, V_{max}/K_{mCDNB} reflects a change in k_2, k_{-2}, or both. If $k_P \gg k_{-2}$, then $V_{max}/K_{mCDNB} = k_2$. If $k_P \ll k_{-2}$, then $V_{max}/K_{mCDNB} = k_P k_2/k_{-2}$. The value of V_{max}/K_{mCDNB} for the mutant protein is significantly lower than the value obtained for GSTM2-2 (see Table 2). This suggests that modification of Met108 to Ala reduces either the kinetic on-rate for CDNB binding ($k_p \gg k_{-2}$) or the affinity constant ($k_P \ll k_{-2}$). Since removal of the side chain of Met108 is not likely to decrease the kinetic on-rate for CDNB binding, k_{-2} is higher in the mutant protein, leading to a reduction in the affinity constant for CDNB. Note that altering Met108 to Ala also increases the turnover number of the enzyme, suggesting that Met108 contributes to the relatively slow off-rate of GSDNB from the wild-type enzyme.

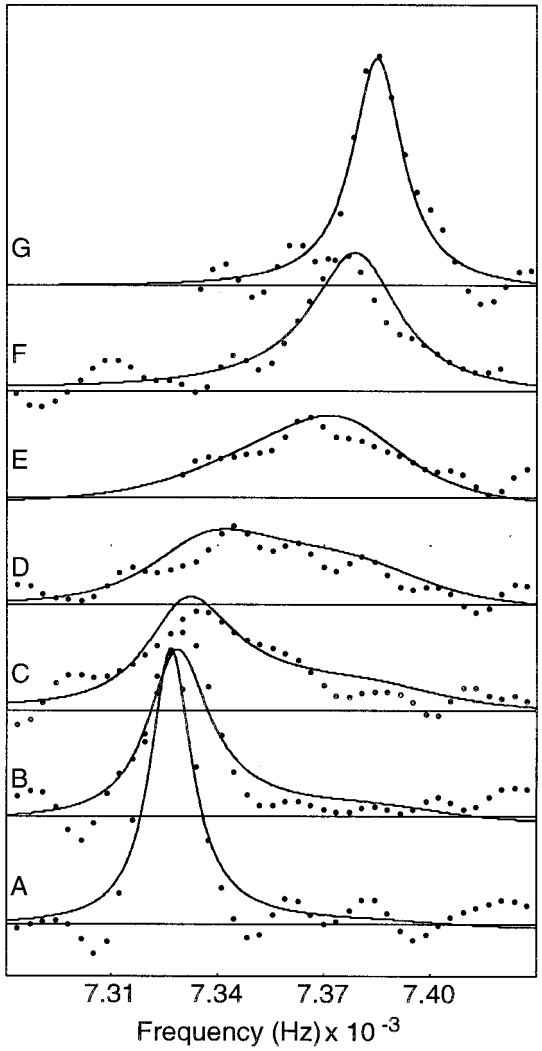

FIGURE 4: Kinetic on- and off-rate constants from line shape analysis of GSDNB binding. The resonance line from Lys49 is shown. The spectral data (dots) and the fitted line shapes are shown for GSDNB concentrations of 0.00 (A), 0.12 (B), 0.28 (C), 0.43 (D), 0.61 (E), 0.80 (F), and 1.18 mM GSDNB (G).

Dynamic Properties of GSTM2-2. On- and Off-Rates As Determined by Line Shape Analysis. Kinetic on-rate constants for the binding of the substrate (GSH), a product (GSDNB), and an inhibitor (GSHEX) were determined by analysis of the line shape of protein amide resonances at different ligand concentrations. Although it is possible to use signals from the ligand for this measurement, the observation of resonances from a number of different residues within the binding pocket of the protein may permit the detection of multistep binding events; however, none were observed here.

Figure 4 shows one-dimensional spectral line shapes for Lys49 that were extracted from $^{15}N-^{1}H$ HSQC spectra acquired at various GSDNB concentrations. The measured kinetic on-rate constants for all ligands are not significantly different; the average is $(1.3 \pm 0.7) \times 10^7$ M^{-1} s^{-1}. The average kinetic off-rate for GSDNB is 190 ± 43 s^{-1}. GSH exhibited a slower off-rate, 100 ± 43 s^{-1}. GSHEX exhibited the slowest off-rate, 30 ± 25 s^{-1}. The large error in the determination of the off-rate of GSHEX is due to the fact that the contribution of chemical exchange to the line width is similar to the natural line width. The measured off-rate for GSDNB is similar to the turnover number of this enzyme, 220 s^{-1} (see Table 2). This similarity suggests that the rate-limiting step in the reaction with CDNB is product release. A similar result has been reported for the homologous rat enzyme, rGST3-3. However, the rate of GSDNB release from GSTM2-2 (190 s^{-1}) is more rapid than the off-rate found in rGSTM3-3 (20 s^{-1}) or for the Tyr115 to Phe mutant of rGSTM3-3 (72 s^{-1}), suggesting that the active site cleft of GSTM2-2 is more open than in the homologous rGSTM3-3 enzyme. This conclusion is supported by the observation that the second-order rate constant (k_{cat}/K_M) for CDNB in the reaction catalyzed by rGST3-3 (10^6 M^{-1} s^{-1}) is an order of magnitude lower than that observed for the binding of *all* ligands to GSTM2-2 (*19*).

The kinetic on-rate for ligand binding to GSTM2-2 is 10−20-fold lower than the diffusion limit of approximately 10^8 M^{-1} s^{-1} (*51*). Kinetic on-rates that are slower than the diffusion limit can be rationalized in several ways. It is possible that the average structure of the protein is not competent for binding of the ligand and a small fraction of the protein exists in alternative conformations that can bind the ligand at the diffusion limit. These two structural subpopulations must interconvert rapidly since there is no spectral evidence for multiple conformations in solution. Alternatively, apparently slow kinetic on-rate constants may indicate multistep binding with a slow conformational change of the protein after the initial collisional encounter. For either binding model, the slow on-rates imply that GSTM2-2 undergoes molecular motion and that this motion is reflected in enzyme function. Residue specific characterization of the dynamic properties of GSTM2-2 were probed by measurement of nuclear spin relaxation, averaging of residual dipolar coupling, and amide exchange kinetics.

Nuclear Spin Relaxation. The ^{15}N relaxation parameters (T_1, T_2, and hnNOE) were obtained for backbone amide groups of unliganded GSTM2-2 and GSTM2-2 in complex with GSH, GSDNB, and GSHEX. Approximately 80% of the observable resonance peaks were detected with adequate sensitivity and resolution for relaxation analysis. The average signal-to-noise ratio in the T_1 and T_2 experiments was approximately 20:1 and 30:1 at 600 and 750 MHz, respectively. The hnNOE measurements were less sensitive, and the signal-to-noise ratio in these spectra was approximately 20:1 at 600 MHz and 15:1 at 750 MHz.

Representative T_2 decay curves are shown in Figure 5. The residue with the longest T_2 is Ser89. The T_1, T_2, and hnNOE were similar for most residues, exhibiting a variation of less than 10%. A few residues exhibited T_2 and hnNOE values indicative of flexibility; these residues are located in the N-terminus and in the loop containing Ser89 (residues 80−90). This loop joins the amino-terminal domain to the carboxy-terminal domain. Interestingly, the residues that comprise the GSH and hydrophobic binding sites of GSTM2-2 do not exhibit any dynamic behavior.

Surprisingly, the ^{15}N relaxation data were largely unchanged upon formation of a complex with GSH, GSDNB, or GSHEX. For example, Trp214 is located in the C-terminal Ω-loop which likely interacts with the hydrophobic portion of GSDNB and GSHEX. However, no significant changes in T_1, T_2, or hnNOE of Trp214 are detected upon binding these ligands (data not shown). Although there were no obvious trends detected in the relaxation data, several interesting correlations were identified using the model-free

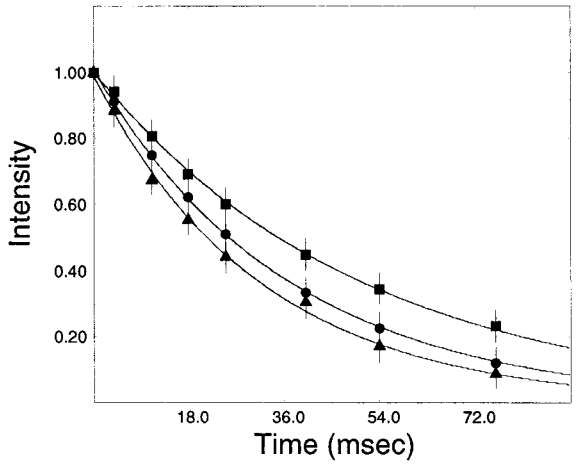

FIGURE 5: T_2 relaxation data. The cross-peak intensity and best-fit curves for residues Ser89 (■), Ala37 (●), and Tyr115 (▲) in unliganded GSTM2-2 are shown.

analysis. Prior to obtaining values for the order parameter (S^2), internal correlation time τ_F, and the chemical exchange term (R_{ex}), we calculated the overall molecular correlation time τ_M according to the methodology described by Kay and co-workers using trimmed values of T_1/T_2 (*52*). The average rotational correlation time for all forms of the enzyme was 24.2 ± 0.3 ns. The small variation in τ_M is attributed to small differences in either the viscosity or temperature between samples. In subsequent model fitting, the overall rotation of the protein was assumed to be isotropic.

The relaxation data for approximately 80% of the residues are best fit with the simplest model for internal motion. This model incorporates a generalized order parameter (S^2) with the assumption that the internal motion has a very fast time component on the sub-picosecond time scale. When a nanosecond to picosecond internal correlation time (τ_F) is incorporated into the motional model, half of the remaining residues gave significantly improved χ^2 values for both unliganded and liganded GSTM2-2. The χ^2 values for almost all of the remaining residues improved with the incorporation of the chemical exchange term R_{ex}. One or two residues exhibit a significant reduction in χ^2 with the incorporation of both the chemical exchange term and the internal correlation time.

The physical interpretation of R_{ex} is complicated by differences in the CSA tensor from residue to residue (*53*). Therefore, no significance was inferred from the R_{ex} values, but their inclusion in the fitted model is important for obtaining accurate values for the other parameters. Consequently, only the order parameter and internal correlation times will be discussed further.

The values for S^2 are shown in Figure 6 for each residue in unliganded GSTM2-2 (panel A). The values for the order parameter exhibit a homogeneous distribution of values that range from approximately 0.86 to 1.00 throughout the entire GSTM2-2 molecule. The few residues with values ranging from 0.65 to 0.86 are found in either the amino terminus (residues 2−5) or the loop segment that connects the two domains (residues 80−90). The high S^2 values provide strong evidence that the backbone is relatively rigid and free of large-amplitude structural fluctuations on the nanosecond to picosecond time scale.

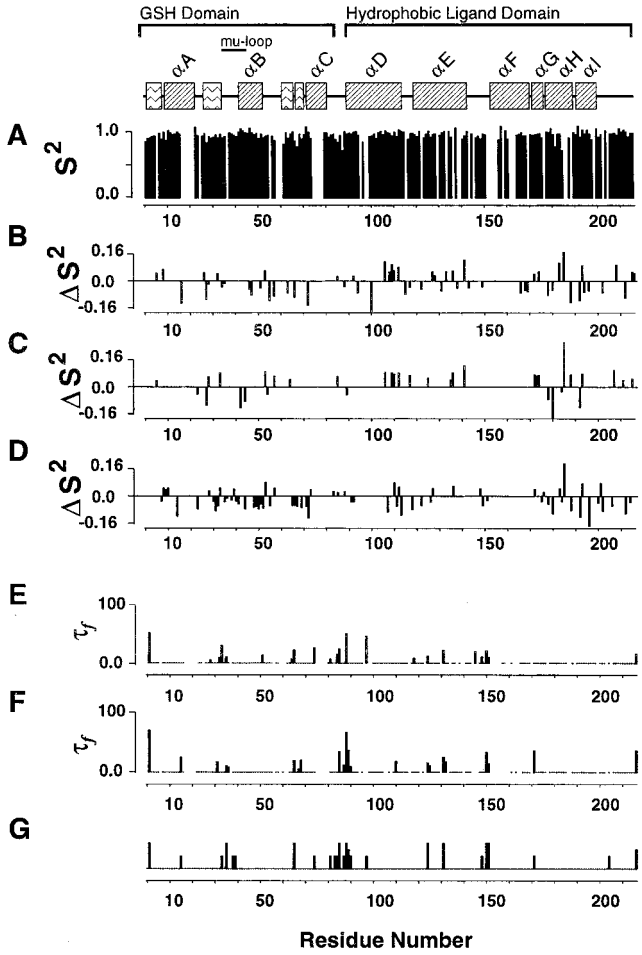

FIGURE 6: Effects of ligand binding on order parameters and internal correlation times. The secondary structure and domain organization of GSTM2-2 are shown in the top part of the figure. Panel A shows the order parameter (S^2) as a function of residue number for unliganded GSTM2-2. Missing bars represent residues without data. Panels B and C show significant differences in the order parameter ($\Delta S^2 = S_{ligand}^2 - S_{unliganded}^2$) as a function of residue number for GSH (B), GSDNB (C), and GSHEX (D). Missing bars indicate that no significant difference between the two order parameters was observed. A line has been drawn through $\Delta S^2 = 0$. The internal correlation time, τ_F (picoseconds), is shown for unliganded (E) and GSTM2-2 in complex with GSHEX (F). Panel G shows an incidence plot. In this plot, the tallest bars represent residues for which a τ_F term was required in all four cases (unliganded, GSH, GSDNB, and GSHEX). The height of the bar for residues which required a τ_F term in only one case is 0.

Addition of ligand to GSTM2-2 does not cause any large-scale changes in the order parameter. Figure 6 (panels B−D) shows the difference in order parameter between the liganded and unliganded GSTM2-2. Although a number of residues exhibit changes in S^2 in the range of 0.1, no obvious trends in the data are apparent. Therefore, there is no evidence for ligand-induced flexibility, on the time scale of picoseconds, for the backbone atoms in the residues that comprise the hydrophobic binding site.

Internal correlation times (τ_F) are shown in Figure 6 for unliganded GSTM2-2 (panel E) and the GSHEX complex (panel F). Similar results (data not shown) were obtained for the GSH and GSDNB complexes. An incidence plot was constructed to readily identify those residues that consistently required a τ_F term in the fitting of the relaxation data (Figure

6G). This plot clearly shows that residues 35−40, 84−90, 125, 132, 151, and 152 exhibit motion on the picosecond to nanosecond time scale. Most of these regions are surface loops. Residues 35−40 are contained within the mu-loop; residues 84−90 join the two domains of the enzyme, and residues 151 and 152 link helices E and F. Residues 125 and 132, which are on the surface-exposed face of the E-helix, also show a consistent requirement for τ_F in the model fitting, suggesting that the central part of this helix exhibits some high-frequency motion. Since the order parameters for *all* residues requiring a τ_F term are close to 1, their motions must be of low amplitude. The remaining residues in the protein do not seem to show any obvious trends in τ_F or ligand-induced changes in τ_F.

It is interesting to note an increase in the number of residues in the interdomain linker (residues 85−90) that require a τ_F term after ligand binding (e.g., compare panel E of Figure 6 to panel F). This observation suggests that ligand binding results in a slight shift in the orientation of the two domains in a manner that enhances the flexibility of this region. A change in the orientation of the two domains is supported by chemical shift changes induced by binding of GSH (see Figure 1). Furthermore, a comparison of the crystal structures of unliganded GSTM2-2 (2gtu) and the GSDNB−GSTM2-2 complex shows a change in the relative orientation of the two domains. This ligand-induced conformational change can be described as a rotation of approximately 2° about an axis that is perpendicular to the overall *C*2 symmetry axis. Although there are a number of small differences in the ϕ and ψ angles of residues 85−90 between the two crystal structures, it is not clear how the mobility of this loop is enhanced by these changes.

The measured order parameters indicate that all of the elements in the hydrophobic binding site of GSTM2-2 are essentially rigid. Residues in the tip of the mu-loop (residues 35−40) exhibit highly restricted motion ($S^2 > 0.85$) with a slower internal correlation time in 1−20 ns range. These results extend earlier work (*18*) that utilized solely hnNOE data to characterize the motional properties of the carboxy-terminal Ω-loop. Although mobility on the 1−20 ns time scale is seen for some surface residues (35−40, 85−90, 126, 132, 151, and 152), these residues are distant from the active site. Therefore, high-frequency motions of the peptide backbone are not likely to provide broad substrate specificity or have an effect on the chemical step of the catalytic cycle of this class mu GST.

Residual Dipolar Coupling. Motion that occurs on a time scale that is shorter than microseconds will average the amide ($^{15}N-^{1}H$) residual dipolar coupling. The degree of averaging depends on the order parameter (S^2) of the motion; under rapid isotropic motion, the observed residual dipolar coupling is zero. Since the nuclear spin relaxation data show that the protein is essentially rigid on the picosecond to nanosecond time scale, any mobility detected by dipolar coupling should report on the time scale in the nanosecond to microsecond range. Motions on this time scale may be important for substrate access to the active site and/or rearrangement of the hydrophobic binding site to accommodate different substrates.

Residual dipolar couplings were measured for partially aligned samples of the unliganded protein and the GSHEX−GSTM2-2 complex. The axial and rhombic components were

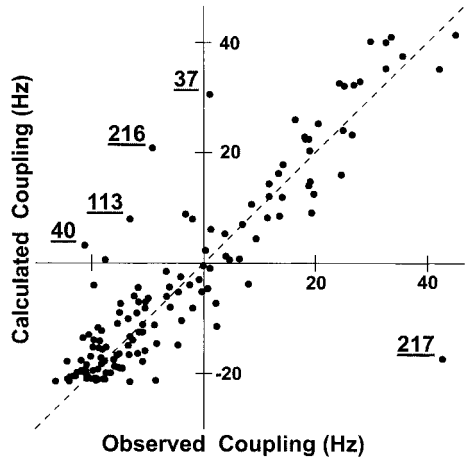

FIGURE 7: Observed vs calculated residual dipole coupling. A scatter plot of the observed vs the calculated residual dipolar couplings is shown for the complex between GSTM2-2 and GSHEX. The dashed line with a slope of unity indicates the expected relationship predicted from the crystal structure. Labels for the points associated with the five residues which exhibit the largest deviation from this relationship are underlined. The remaining points are not labeled. The calculated dipole couplings were obtained from the re-refined structure of GSTM2-2 complexed with GSDNB. The GSHEX complex was modeled by replacement of the DNB ring with the hexyl group from a homologous class mu enzyme (*10*). The average change in the position of the backbone atoms after energy minimization of this model was less than 0.05 Å; the largest deviation was 0.18 Å for residue 37.

−13.0 and 3.2 Hz in the case of the unliganded protein and −21.8 and 1.4 Hz for the GSHEX−GSTM2-2 complex. In both cases, the rhombic component is small, and not significantly different from zero.

A scatter plot of calculated versus measured dipolar couplings for the GSHEX−GSTM2-2 complex is shown in Figure 7. For *both* the unliganded and GSHEX samples, a number of residues exhibited deviations significantly greater than expected from experimental error. These include the last two residues of the carboxy terminus (Asn216 and Lys217), the end of the D-helix (Leu113), and residues in the mu-loop (Ala37 and Tyr40). The differences between the experimental and predicted dipolar coupling for residues 216 and 217 cannot be resolved at this time. The conformation of the Ω-loop is poorly defined by the electron density (temperature factors exceed 60 $Å^2$), and the conformation of these residues in the NMR structure is ill-defined due to a small number of distance constraints. Although the structure of these terminal residues is currently unknown, it is important to note that these residues are ordered; their order parameters (S^2) on the picosecond to nanosecond time scale are close to 1, and their measured residual dipolar couplings are clearly not zero.

The conformation of residues 113−118 (D-helix) appears to be different in solution and in the crystal structure of the GSDNB−GSTM2-2 complex since the predicted and measured residual dipolar couplings differ by more than 3 times the standard error of the measurement. These differences are likely due to a distortion of the top of the D-helix by packing in the crystal lattice. The predominate conformation of the top of the D-helix appears to be similar to that observed in the unliganded GSTM2-2 crystal structure (2gtu). The dipolar couplings predicted for residues 113−118 from this crystal structure are within experimental error of the measurement.

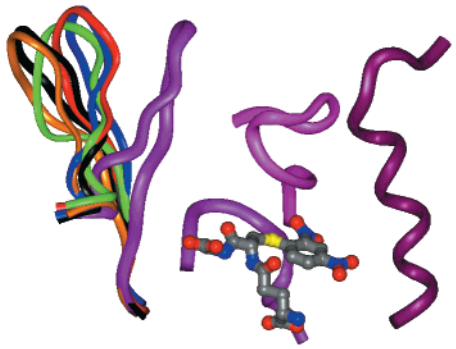

FIGURE 8: Alternative structure of the mu-loop determined from residual dipolar couplings. This figure only shows sections of the protein that surround the active site. The mu-loop is the left-most structural element. The D-helix is the right-most structure. The carboxy terminus is located between the mu-loop and the D-helix. The floor of the active site is located below the carboxy terminus and behind the bound ligand (CPK coloring). The conformation of the protein as defined by the crystal structure of the GSDNB complex is colored magenta. The five additional conformations of the mu-loop generated from molecular mechanics calculations that give the best agreement between the measured and calculated dipolar couplings are colored blue, red, green, black, and orange.

The dipolar couplings for residues 37 and 40 suggest that the mu-loop also has a different conformation in solution. In addition, the observed dipolar coupling of zero for residues 37 and 39 may indicate motional averaging of the dipolar coupling constant. To determine if alternative conformations of the mu-loop could account for the observed dipolar couplings, an ensemble of 200 structures was generated using molecular mechanics calculations. The five structures whose predicted residual dipolar coupling were closest to the experimental couplings are shown in Figure 8. The position of the mu-loop in these structures corresponds to a rigid tilt of the tip of the mu-loop of about 30° from its position in the crystal structure. This degree of tilt is likely to be exaggerated because a steric clash between Tyr40 (on the mu-loop) and Met211 tends to cause a displacement of the mu-loop away from the active site region. Nevertheless, it appears that in solution the mu-loop is displaced outward from the conformation observed in the crystalline form, facilitating access to the active site region of the enzyme.

Although the molecular mechanics calculation yielded structures that exhibited a better overall agreement to the measured couplings, none of these structures can account for the observed couplings of zero for residues 37 and 39. The absolute values of the coupling for these residues ($|D_{ij}|$), when averaged over the best five structures, are 6.1 and 3.1, respectively (see Table 3). However, if the calculated dipolar couplings for each residue in the five best structures are averaged to account for rapid interconversion between structures, a coupling constant of ~0 is obtained for residues 37 and 39 (see Table 3, fourth column). This analysis suggests that a single conformation of residues 37−39 cannot account for the observed coupling and that conformations like those shown in Figure 8 are averaged to produce the observed coupling. The time scale for this averaging of the coupling is most likely the microsecond to nanosecond range. However, in some restricted situations, it is possible to obtain an apparent averaging of the coupling on a time scale slower than microseconds. If the time scale of the conformational change is sufficiently rapid to average the chemical shift of a residue (i.e., microseconds to milliseconds), then the observed evolution of the J coupling will be equal to the sum of $\cos(\pi Jt)$ for each conformer. If the differences between the individual residual dipolar couplings for each conformer are small, then the resultant sum will be experimentally fit to a single cosine function whose J coupling value is close to the mean value. An identical type of averaging also occurs for conformational changes that occur on a time scale longer than milliseconds. This situation is much more restrictive, requiring little or no change in the chemical shifts for the residue due to the conformational change. Otherwise, separate resonance lines, each with its own dipolar coupling, would be observed for each individual conformer.

Table 3: Residual $^1H-^{15}N$ Dipolar Couplings (Hertz) for Different Conformational Models of the Mu-Loop[a]

residue no.	observed D_{ij}	X-ray D_{ij}	average D_{ij}	average $\|D_{ij}\|$
32	18.2	18.1	12.2	12.2
33	3.4	2.7	3.4	5.7
35	−7.0	−0.7	−3.8	4.2
36	16.3	18.6	8.1	8.1
37	1.1	14.0	−1.2	6.1
39	−0.5	0.4	0.0	3.1
40	−8.5	1.2	−5.5	5.5
41	−7.2	−8.0	−8.7	5.1
42	−9.6	−9.4	−4.7	4.7

[a] These results are for unliganded GSTM2-2. Similar values (scaled by the ratio of the A_a values) were obtained for the GSHEX−GSTM2-2 complex. The conformational models were generated by molecular mechanics calculations using the unliganded crystal structure (2gtu). Definitions: observed D_{ij}, experimentally observed residual dipolar coupling; X-ray D_{ij}, dipolar coupling predicted from the unliganded X-ray structure (2gtu); average D_{ij}, averaged residual dipolar coupling for the five structures that gave the best agreement with the observed D_{ij}; average $|D_{ij}|$, average of the absolute value of the residual dipolar coupling for the same five structures.

Table 4: Amide Exchange Kinetics[a]

residue no.	τ(no ligand)	τ(GSH)	RGSH	τ(GSHEX)	RGSHEX
9	4.7 ± 0.5	20.2 ± 1.5	4.3	77.0 ± 6.0	16.3
10	4.4 ± 0.4	18.0 ± 1.7	4.1	19.1 ± 2.2	4.4
13	1.4 ± 1.0	23.1 ± 3.4	16.5	68.9 ± 3.0	49.1
105	3.6 ± 0.6	25.9 ± 4.5	7.2	79.9 ± 12.3	22.2
107	1.1 ± 0.6	22.7 ± 4.2	20.1	ND	ND
108	9.5 ± 0.6	21.8 ± 4.3	2.3	92.9 ± 19.5	9.8
112	9.3 ± 0.7	14.6 ± 1.6	1.6	57.1 ± 4.3	6.1
113	18.2 ± 2.4	15.2 ± 1.8	0.8	128.6 ± 12.0	7.0
115	11.6 ± 3.4	ND	ND	59.5 ± 7.5	5.1
116	13.3 ± 1.1	ND	ND	58.9 ± 3.4	4.4
123	27.1 ± 2.7	43.3 ± 8.0	1.7	88.3 ± 6.9	3.3
127	18.6 ± 1.8	27.7 ± 3.3	1.5	70.2 ± 11.8	3.8
136	5.3 ± 0.5	8.8 ± 1.2	1.7	23.7 ± 2.0	4.5
137	46.1 ± 9.2	30.2 ± 4.2	0.7	141.4 ± 26.0	3.1
196	1.8 ± 1.1	ND	ND	53.9 ± 5.2	29.6
208	0.5 ± 0.3	5.2 ± 0.7	11.3	6.5 ± 0.7	14.2
213	1.7 ± 0.7	1.1 ± 0.3	0.6	15.5 ± 1.5	9.1
214	1.6 ± 1.3	8.9 ± 1.7	5.5	17.5 ± 1.5	10.9

[a] The amide hydrogen lifetimes, τ (hours), are shown for residues that have a significant increase in lifetime in the presence of either GSH or GSHEX. Columns labeled R give the ratio of the amide lifetime for liganded vs unliganded GSTM2-2. ND, not determined.

Amide Exchange. Amide exchange rates for unliganded GSTM2-2 and the GSHEX complex are provided in Table 4. It was possible to compare amide exchange rates for 50 residues. The distribution of these residues in the structure of GSTM2-2 is shown in Figure 9. The remaining residues

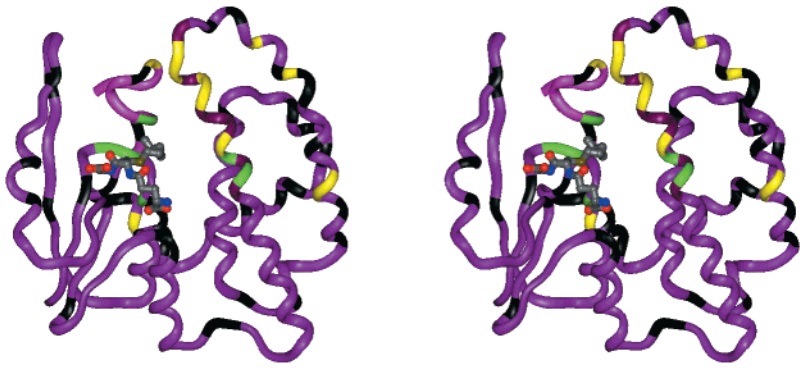

FIGURE 9: Amide exchange kinetics. Residues that exhibit a reduction in amide exchange rates due to binding of GSH or GSHEX are mapped on the structure of GSTM2-2. For reference, bound GSHEX is included in the figure. This structure was modeled as described in the legend of Figure 7. The mu-loop is the left-most structural element. The D-helix is slightly to the right of the center of the molecule. The carboxy terminus is located between the mu-loop and the D-helix. The floor of the active site is below the carboxy terminus. The bound GSHEX is rendered as a ball-and-stick model (CPK coloring). Residues for which amide exchange could be measured are colored black, green, or yellow. Residues that exhibited a reduction in the rate of amide exchange due to GSH binding are colored green. Residues that exhibited a reduction in the rate of exchange due to GSHEX binding are colored green and yellow (with the exception of residue 107, whose exchange properties were not determined for GSHEX). This figure is drawn in relaxed stereo and was produced using InsightII.

were not resolved, exchanged too rapidly or too slowly, or could not be assigned in both the unliganded protein and the GSH and GSHEX complexes. Residues were not considered to have significantly different amide exchange rates in the enzyme−ligand complexes unless their mean rates differed by more than five standard deviations. Ligand-induced changes in amide exchange rates that were at least 3-fold slower in the GSH or GSHEX complex than in the unliganded protein are shown in Table 4. The locations of these residues within the protein structure are highlighted in Figure 9.

Binding of GSH reduced the amide exchange rates of a number of residues in proximity to the bound ligand. The observed reduction in exchange rates for residues 9, 10, 13, and 208 is likely due to the fact that the bound GSH would hinder access of the solvent to these residues. In contrast, residues 105, 107, and 214 show a decrease in the exchange rates in the presence of GSH but are distant from the bound ligand. Therefore, GSH binding must reduce the mobility of the D-helix and carboxy-terminal regions. This effect is largest for residues in the central portion of the D-helix (residue 107 exhibits a ratio of 20) and is attenuated toward the ends of the D-helix.

The binding of GSHEX reduces the amide exchange rate of a larger number of residues. Residues that exhibited reduced exchange rates can be divided into several classes on the basis of their proximity to the bound ligand. Residues Ile9, Arg10, Ala13, Met105, and Phe208 either contact the bound ligand or are spatially adjacent to residues that contact either the hydrophobic or glutathione portion of GSHEX. The remaining residues (112, 113, 115, 116, 123, 127, 136, 137, 196, 213, and 214) are distant for the bound ligand. Residues 112−116 and residues 123 and 127 are spatially close to each other at the top of the D-helix and likely report on dynamic changes that alter the exchange properties of the D-helix upon ligand binding. Resides 136 and 137 are part of the E-helix. Although this helix contacts the D-helix, it is more likely that their exchange properties are due to the presence of ligand bound to the active site in the symmetry-related monomer. Residues 213 and 214 are in the carboxy terminus, and the increase in their exchange lifetime reflects changes in dynamics that may be propagated from Phe208.

Reduction in amide exchange rates due to complex formation can be the result of three factors: desolvation of the amide group due to direct protein−ligand interactions, desolvation due to changes in the average structure, or a reduction in the manifold of conformational states from which exchange can occur. Changes in the average structure do not play a role here for the following reasons. The crystal structures of unliganded GSTM2-2 (2gtu) and the GSDNB−GSTM2-2 complex align with an overall rmsd of 0.6 Å. Residues in the D- and E-helices exhibit a rmsd of 0.42 Å. These small conformational changes suggest that the structure of this region of GSTM2-2 is not greatly affected by ligand binding. There is a more substantial difference between the conformation of residues Val213 and Trp214 in the unliganded and the GSDNB−GSTM2-2 crystal structures (rmsd of 1.1 Å). However, the conformation of this region in the GSDNB−GSTM2-2 structure is not well-defined; consequently, this rmsd may be misleading. Three observations suggest that large ligand-induced structural changes do not occur in the carboxy-terminal Ω-loop. First, the chemical shift changes due to ligand binding are small (average changes are $\omega_N = 0.26$ ppm and $\omega_{HN} = 0.12$ ppm). Second, the NMR structure of the Ω-loop in unliganded GSTM2-2 (*18*) is similar to that observed in the GSDNB−GSTM2-2 crystal structure. Third, the scaled residual dipolar couplings for residues 210−217 in the unliganded sample are similar to those in the liganded sample (see Table 5).

The reduction in the amide exchange rate for residues in the D-helix and in the carboxy terminus suggests that the dynamic properties of these regions change as a result of ligand binding. These changes do not involve high-frequency motions (i.e., microsecond to picosecond time scale) because the order parameters from both NMR spin relaxation measurements and residual dipolar coupling are near unity. Therefore, the motion must involve slow excursions into conformations with elevated amide exchange rates. These excursions are dampened in the presence of ligand, leading to a reduction in the rate of amide exchange.

Table 5: Residual $^{1}H-^{15}N$ Dipolar Couplings (Hertz) for Residues 210−217

residue no.	D_{ij}(no ligand)	D_{ij}(GSHEX)
211	−18.4	−19.9
212	−3.8	−4.6
213	6.8	2.2
214	−18.0	−22.7
215	−15.7	−4.7
216	−7.2	−9.2
217	39.9	42.5
R-factor[a] = 25.6%		

[a] $R = \Sigma|D_{ij}^{\text{noligand}}| - |D_{ij}^{\text{GSHEX}}|/\Sigma|D_{ij}^{\text{GSHEX}}|$.

CONCLUSIONS

Regions of GSTM2-2 that are likely to adopt different conformations have been previously identified on the basis of high crystallographic temperature factors. These regions are the mu-loop, the carboxy terminus, and the top of the D-helix. It is clear from the order parameters that none of these regions undergo motion of significant amplitude on the nanosecond to picosecond time scale. The residual dipolar coupling measurements show that neither the carboxy terminus nor the D-helix experiences motion on the microsecond to nanosecond time scale. In contrast, residual N−H dipolar couplings suggest that the mu-loop samples different conformational states in both liganded and unliganded enzymes on the microsecond to nanosecond time scale. The time scale for the mobility of the mu-loop suggests that this conformational change may be involved in gating the access of substrates to and the release of products from the active site. In addition, these measurements also show that the mu-loop assumes a more open conformation in solution, further facilitating ligand binding and release. This conclusion is supported by the fact that the kinetic off-rate for dissociation of GSDNB from GSTM2-2 is faster than that observed in the homologous enzyme from rat (rGSTM3-3) and that the kinetic on-rate for all ligands (GSH and GSDNB) are 1 order of magnetude faster than that observed for rGSTM3-3.

Amide hydrogen exchange studies show that the D-helix and the Ω-loop undergo motion on a time scale longer than microseconds. The binding of ligand reduces the number of conformational states sampled by the protein. This damping of motion may be important for generating an optimal configuration for the nucleophillic substitution reaction as well as for providing a favorable entropic contribution to the free energy of product release.

The role of dynamics in the generation of substrate specificity is also addressed by these studies. Substrate specificity may be generated from different conformations of the hydrophobic binding site. Although the tip of the mu-loop does sample different conformations, it is too distant to play a direct role in defining substrate specificity. Multiple conformations of the D-helix and the carboxy terminus could play a role in broadening substrate specificity. However, it is apparent from the relaxation measurements and the residual dipolar couplings that significantly different backbone conformations of the D-helix and carboxy terminus are unlikely to exist in solution. Therefore, if the broad substrate specificity of GSTM2-2 is due to the existence of different conformations, these differences must be localized to the side chain atoms of the residues in the active site.

ACKNOWLEDGMENT

We thank Dr. A. Palmer for help with Modelfree as well as for providing FELIX macros for analysis of the raw relaxation data.

SUPPORTING INFORMATION AVAILABLE

Relaxation data and chemical shift assignments. This material is available free of charge via the Internet at http://pubs.acs.org.

REFERENCES

1. Armstrong, R. N. (1997) *Chem. Res. Toxicol. 10*, 2−18.
2. Eaton, D. L., and Bammler, T. K. (1999) *Toxicol. Sci. 49*, 156−164.
3. Salinas, A. E., and Wong, M. G. (1999) *Curr. Med. Chem. 6*, 279−309.
4. Rushmore, T. H., and Pickett, C. B. (1993) *J. Biol. Chem. 268*, 11475−11478.
5. Bruns, C. M., Hubatsch, I., Ridderstrom, M., Mannervik, B., and Tainer, J. A. (1999) *J. Mol. Biol. 288*, 427−439.
6. Cameron, A. D., Sinning, I., L'Hermite, G., Olin, B., Board, P. G., Mannervik, B., and Jones, T. A. (1995) *Structure 15*, 717−727.
7. Sinning, I., Kleywegt, G. J., Cowan, S. W., Reinemer, P., Dirr, H. W., Huber, R., Gilliland, G. L., Armstrong, R. N., Ji, X., Board, P. G., Olin, B., Mannervik, B., and Jones, T. A. (1993) *J. Mol. Biol. 232*, 192−212.
8. Patskovska, L. N., Fedorov, A. A., Patskovsky, Y. V., Almo, S. C., and Listowsky, I. (1998) *Acta Crystallogr., Sect. D: Biol. Crystallogr. 54*, 458−460.
9. Raghunathan, S., Chandross, R. J., Kretsinger, R. H., Allison, T. J., Penington, C. J., and Rule, G. S. (1994) *J. Mol. Biol. 238*, 815−832.
10. Sun, Y. J., Kuan, I. C., Tam, M. F., and Hsiao, C. D. (1998) *J. Mol. Biol. 278*, 239−252.
11. Ji, X., Zhang, P., Armstrong, R. N., and Gilliland, G. L. (1992) *Biochemistry 31*, 10169−10184.
12. Ji, X., Armstrong, R. N., and Gilliland, G. L. (1993) *Biochemistry 32*, 12949−12954.
13. Oakley, A. J., Lo Bello, M., Ricci, G., Federici, G., and Parker, M. W. (1998) *Biochemistry 37*, 9912−9917.
14. Reinemer, P., Dirr, H. W., Ladenstein, R., Huber, R., Lo Bello, M., Federici, G., and Parker, M. W. (1992) *J. Mol. Biol. 227*, 214−226.
15. Rossjohn, J., McKinstry, W. J., Oakley, A. J., Verger, D., Flanagan, J., Chelvanayagam, G., Tan, K. L., Board, P. G., and Parker, M. W. (1998) *Structure 6*, 309−322.
16. Dirr, H., Reinemer, P., and Huber, R. (1994) *Eur. J. Biochem. 220*, 645−661.
17. Board, P. G., Coggan, M., Wilce, M. C., and Parker, M. W. (1995) *Biochem. J. 311*, 247−250.
18. McCallum, S. A., Hitchens, T. K., and Rule, G. S. (1999) *J. Mol. Biol. 285*, 2119−2132.
19. Johnson, W. W., Liu, S., Gilliand, G. L., and Armstrong, R. N. (1993) *J. Biol. Chem. 268*, 11508−11511.
20. Penington, C. J., and Rule, G. S. (1992) *Biochemistry 31*, 2912−2920.
21. Peng, J. W., and Wagner, G. (1994) *Nuclear Magnetic Resonance Probes of Molecular Dynamics* (Tycko, R., Ed.) pp 373−454, Kluwer Academic Publishers, Dordrecht, The Netherlands.
22. Palmer, A. G. (1997) *Curr. Opin. Struct. Biol. 7*, 732−737.
23. Lipari, G., and Szabo, A. J. (1982) *J. Am. Chem. Soc. 104*, 4546−4559.
24. Clore, G. M., Szabo, A., Bax, A., Kay, L. E., Driscoll, P. C., and Gronenborn, A. M. (1990) *J. Am. Chem. Soc. 112*, 4989−4991.
25. Mandel, A. M., Akke, M., and Palmer, A. G. (1995) *J. Mol. Biol. 246*, 144−163.

26. Bothner-By, A. A., Gayathri, C., van Zijl, P. C. M., Maclean, C., Lai, J.-J., and Smith, K. M. (1985) *Magn. Reson. Chem. 23*, 935−938.
27. Tjandra, N., Omichinski, J. G., Gronenborn, A. M., Clore, G. M., and Bax, A. (1997) *Nat. Struct. Biol. 4*, 732−738.
28. Hansen, M. R., Rance, M., and Pardi, A. (1998) *J. Am. Chem. Soc. 120*, 11210−11211.
29. Tolman, J. R., Flanagan, J. M., Kennedy, M. A., and Prestegrad, J. H. (1997) *Nat. Struct. Biol. 4*, 292−297.
30. Woodward, C. K., and Hilton, B. D. (1979) *Annu. Rev. Biophys. Bioeng. 8*, 99−127.
31. Englanger, S. W., Englander, J. J., McKinnie, E. R., Ackers, G. K., Turner, G. J., Westrick, J. A., and Gill, S. J. (1992) *Science 256*, 1684−1687.
32. Miller, D. W., and Dill, K. A. (1995) *Protein Sci. 4*, 1860−1873.
33. Williams, D. C., Benjamin, D. C., Poljak, R. J., and Rule, G. S. (1996) *J. Mol. Biol. 257*, 866−876.
34. Freire, E. (1999) *Proc. Natl. Acad. Sci. U.S.A. 96*, 10118−10122.
35. Schramm, V. L., McCluskey, R., Emig, F. A., and Litwack, G. (1984) *J. Biol. Chem. 259*, 714−722.
36. Kunkel, T. A., Bebenek, K., and McClary, J. (1991) *Methods Enzymol. 204*, 125−139.
37. Habig, W. H., and Jakoby, W. B. (1981) *Methods Enzymol. 77*, 398−405.
38. Segel, I. H. (1975) *Enzyme Kinetics*, John Wiley, New York.
39. Johnson, M. L., and Frasier, S. G. (1985) *Methods Enzymol. 117*, 301−342.
40. Marion, D., Ikura, M., and Bax, A. (1989) *J. Magn. Reson. 84*, 425−430.
41. Bax, A., and Pochapsky, S. S. (1992) *J. Magn. Reson. 99*, 638−643.
42. Sklenář, V., Piotto, M., Leppik, R., and Saudek, V. (1993) *J. Magn. Reson. 102*, 241−245.
43. Case, D. A. (1995) *J. Biomol. NMR 6*, 341−346.
44. Bax, A., Ikura, M., Kay, L. E., Torchia, D. A., and Tschudin, R. (1990) *J. Magn. Reson. 86*, 304−318.
45. McConnell, H. M. (1958) *J. Chem. Phys. 28*, 430−434.
46. Lian, L.-Y., and Roberts, G. C. K. (1993) in *NMR of Macromolecules* (Roberts, G. C. K., Ed.) pp 153−182, IRL Press, Oxford, U.K.
47. Farrow, N. A., Muhandiram, R., Singer, A. U., Pascal, S. M., Kay, C. M., Gish, G., Shoelson, S. E., Pawson, T., Forman-Kay, J. D., and Kay, L. E. (1994) *Biochemistry 33*, 5984−6003.
48. Hansen, M. R., Mueller, L., and Pardi, A. (1998) *Nat. Struct. Biol. 5*, 1065−1074.
49. Tjandra, N., Grzesiek, S., and Bax, A. (1996) *J. Am. Chem. Soc. 118*, 6264−6272.
50. Brunger, A. T. (1992) *X-PLOR, A system for X-ray Crystallography and NMR*, Yale University Press, New Haven, CT.
51. Fersht, A. (1985) *Enzyme Structure and Mechanism*, Freeman Press, New York.
52. Kay, L. E., Torchia, D. A., and Bax, A. (1989) *Biochemistry 28*, 8972−8979.
53. Fushman, D., Tjandra, N., and Cowburn, D. (1998) *J. Am. Chem. Soc. 120*, 10947−10952.

BI992767D